Applied Surface Science 501 (2020) 143973

Contents lists available at ScienceDirect

Applied Surface Science

journal homepage: www.elsevier.com/locate/apsusc

Full Length Article

Similarity in ruthenium damage induced by photons with different energies: From visible light to hard X-rays

I. Milov[a,*], V. Lipp[b], D. Ilnitsky[c], N. Medvedev[d,e], K. Migdal[c], V. Zhakhovsky[c,f], V. Khokhlov[g], Yu. Petrov[g,h], N. Inogamov[f,g], S. Semin[i], A. Kimel[i], B. Ziaja[b,j], I.A. Makhotkin[a], E. Louis[a], F. Bijkerk[a]

[a] Industrial Focus Group XUV Optics, MESA+ Institute for Nanotechnology, University of Twente, Drienerlolaan 5, 7522 NB Enschede, the Netherlands
[b] Center for Free-Electron Laser Science CFEL, Deutsches Elektronen-Synchrotron DESY, Notkestrasse 85, 22607 Hamburg, Germany
[c] Dukhov Research Institute of Automatics, Sushchevskaya 22, Moscow 127055, Russia
[d] Institute of Physics, Czech Academy of Sciences, Na Slovance 2, 182 21 Prague 8, Czech Republic
[e] Institute of Plasma Physics, Czech Academy of Sciences, Za Slovankou 3, 182 00 Prague 8, Czech Republic
[f] Joint Institute for High Temperatures, Russian Academy of Sciences, Izhorskaya 13 Bldg.2, Moscow 125412, Russia
[g] Landau Institute for Theoretical Physics, Russian Academy of Sciences, Chernogolovka 142432, Russia
[h] Moscow Institute of Physics and Technology, Institutskiy Pereulok 9, Dolgoprudny, Moscow Region 141700, Russia
[i] Institute for Molecules and Materials, Radboud University Nijmegen, Nijmegen 6525 AJ, the Netherlands
[j] Institute of Nuclear Physics, Polish Academy of Sciences, Radzikowskiego 152, 31-342 Krakow, Poland

ARTICLE INFO

Keywords:
Femtosecond laser ablation
X-ray free electron lasers
Monte Carlo simulations
Two-temperature hydrodynamics
Thin films
Extreme ultraviolet

ABSTRACT

We performed combined experimental and computational research on damage processes in ruthenium thin films induced by femtosecond lasers with various photon energies. We present an experiment with an optical laser at normal incidence conditions and compare it with previously reported experiments at grazing incidence conditions with XUV and hard X-ray photons, covering a large range of photon energies. Analysis of ablation craters in Ru shows very similar crater morphology and depth of about 10–20 nm for all considered irradiation conditions. Simulations of light-matter interactions are performed with our combined Monte Carlo and two-temperature hydrodynamics approach. The simulation results show that the primal cause of eventual ablation is Auger decay of core-shell holes created after absorption of XUV and hard X-ray photons in the vicinity of ruthenium surface. They lead to the creation of many low-energy electrons which consequently release the absorbed energy near the surface, resembling the optical irradiation case. Similar absorbed energy distributions in the top part of ruthenium induce a similar thermo-mechanical response and, therefore, similar ablation process. Our results suggest that such mechanism is universal in a wide range of photon energies at grazing incidence conditions, when the photon absorption depth is smaller than the photoelectrons range.

1. Introduction

Interaction of femtosecond laser pulses with matter is a complex multi-physical and multi-scale process, which strongly depends on the irradiation conditions and the target properties. Understanding the mechanisms that govern such interactions is of crucial importance in both fundamental and applied science. Absorption of intense femtosecond laser pulses can bring material into an excited non-equilibrium state at considerably high temperature (up to several eV), but still at solid state density. The theoretical description of such a state, also referred to as warm dense matter [1,2], is challenging, since neither standard solid state nor semi-classical plasma formalisms can be directly applied [3,4]. Relaxation of such an excited system may lead to strong changes in the lattice structure of the irradiated target and eventually to severe damage. Identifying and controlling such processes is necessary, e.g., to manufacture long lasting reflective optics for the rapidly developing X-ray free-electron lasers (XFELs).

A typical damage phenomenon that occurs after irradiation of a target with intense femtosecond laser pulses is ablation of the top surface material. Many studies of laser ablation in solids with optical lasers were performed in the past [5–10]. Damage tests of different materials such as multilayer mirrors [11–13], thick substrates [14–16] and thin films [12,14–19] at extreme ultraviolet (XUV) and X-ray free electron laser light sources were also reported. Although such

---

[*] Corresponding author.
E-mail address: i.milov@utwente.nl (I. Milov).

https://doi.org/10.1016/j.apsusc.2019.143973
Received 1 August 2019; Received in revised form 30 August 2019; Accepted 11 September 2019

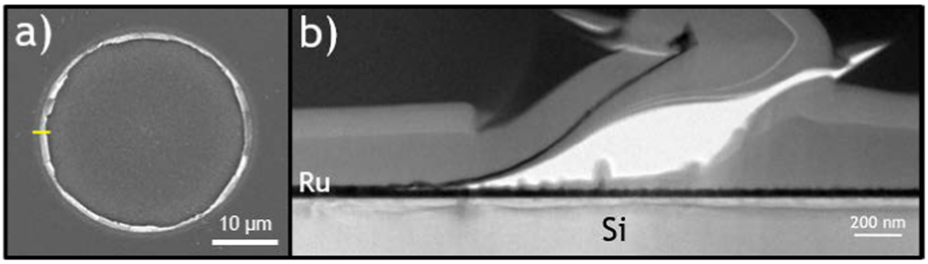

Fig. 1. (a) SEM image of Ru damage crater produced by a 90 fs 1.5 eV (800 nm) laser pulse with an incident peak fluence $F = 500\ \mathrm{mJ/cm^2}$. The yellow line indicates where the TEM cross-section is made. (b) TEM cross-section image taken at the edge of the damage crater, illustrating ablation of the top 15–20 nm of Ru. (For interpretation of the references to colour in this figure legend, the reader is referred to the web version of this article.)

experiments at XFELs are becoming more and more accessible, there is still a lack of detailed understanding of the nature of the observed damage phenomena. Moreover, scalability of already known results to different materials and irradiation conditions is of high demand in order to avoid numerous experimental tests.

Thin metal films are commonly used as grazing incidence mirrors at XFEL facilities to ensure high reflectivity. At such conditions light is absorbed in the thin (several nm) top layer of the target, which is similar to the well-studied optical case, where absorption occurs within the skin depth of about 10 nm. Despite that similarity in the photoabsorption depth, the following evolution of excited electrons strongly depends on the incident photon energy. In a metal, an optical laser only probes conduction band electrons due to low energy of the incident photons. Excitation of core electrons is possible only via multi-photon absorption which requires extremely high intensities. Contrarily, in the X-rays regime the photons are predominantly absorbed by core-shell electrons. As a result, secondary electrons with various kinetic energies are created, which can play a role in the damage processes in the target [20–22].

In the present paper, we perform an experimental and theoretical comparative study of single-shot damage produced in ruthenium (Ru) films by femtosecond laser pulses in a wide photon energy range, from the optical to the hard X-ray regime. Ru is chosen as a relevant material to be used as a grazing incidence reflective mirror at XFEL facilities [15,21,23]. Four different photon energies are compared, namely 1.5 eV (optical), 92 eV (XUV), 7 and 12 keV (hard X-rays). The XUV single-shot damage experiment was reported by Milov et al. in previous work [23], while for 7 and 12 keV we analyze the data from the work by Aquila et al. [21,24]. The optical damage experiment is performed in the present work.

The complex nature of light-matter interaction dictates the necessity to use a combination of different models to describe various physical aspects involved in such interaction. For example, a combination of the two-temperature-based models with classical molecular dynamics is frequently used to describe the interaction of the optical lasers with the targets [25,26]. In the Ref. [22] an approach of combining hydrodynamics simulations with calculations of the radiation field in the material was applied to model the XFEL-matter interaction.

In our work, the experimental results are analyzed using a two-temperature hydrodynamics (2T-HD) model [27], which simulates material response to ultrafast energy deposition. The latter is obtained with the Monte Carlo code XCASCADE(3D) [28], which models the photoabsorption and subsequent non-equilibrium electron kinetics. Such an approach combining the Monte Carlo and 2T-HD methods provides insights into the spatial distributions of material characteristics inside a heated sample during its evolution, starting from photoabsorption and non-equilibrium electron cascades, up to the lattice response and damage formation.

To successfully apply the 2T-HD model, the equation of state (EOS) of the material under investigation is required. Ru is still poorly studied in the two-temperature (2T) regime of thermal non-equilibrium between electrons and ions, which is realized after the absorption of a femtosecond laser pulse. In a separate paper [29] we obtain the 2T EOS that govern the thermodynamics of Ru in a wide range of temperatures and pressures using *ab initio* density functional theory (DFT) calculations. The kinetic coefficients (2T thermal conductivity and electron-phonon coupling factor) are also calculated in [29].

2. Experiment

Optical single-shot damage experiments were performed using a femtosecond regenerative amplifier system (Spectra Physics Spitfire, 800 nm wavelength, maximum energy of 2.2 mJ at 1 kHz, ~90 fs FWHM pulse length) under atmospheric conditions. For the damage experiment the laser system was operated in single-shot mode, which allows only one laser pulse to be released after the trigger event. For beam characterization, the laser system was operated in multi-shot mode, where pulses were released at 1 kHz repetition rate.

The p-polarized laser beam was focused on a sample into a spot of ~42 µm radius (radius @ $1/e^2$). The beam radius was characterized by the knife edge method along the horizontal direction. The sample was positioned slightly before the focal spot to avoid possible ionization of air and, therefore, disturbance of the beam quality at the sample. The angle of incidence (AOI) was set close to normal (~10° off-normal). To continuously control the laser fluence we used an attenuator comprising a half-wave plate and a polarizer. We characterized the laser pulse duration by locating an autocorrelator just before the sample, with typical measured values to be ~90 fs (FWHM).

A Ru polycrystalline film of 50 nm thickness was used as a target. The sample was prepared by depositing Ru on a naturally oxidized super-polished silicon substrate using the magnetron sputtering technique. Irradiations were performed varying the incident fluence. For each fluence a pristine surface was irradiated.

Ex situ analysis was performed by means of scanning electron microscopy (SEM) and transmission electron microscopy (TEM). Fig. 1(a) shows a SEM image of a typical damage crater produced during the experiment described above. Ablation, also referred to as thermo-(photo-) mechanical spallation, of the top part of Ru is observed, which is typical for metals irradiated with high fluence femtosecond optical lasers [26,30–34]. The remaining part of the ablated Ru forms the edge of the crater. The surface at the bottom of the crater appears to be much rougher, compared to the non-irradiated surface. The fact that only the top part of the Ru layer is ablated is confirmed by TEM measurements. Fig. 1(b) shows a TEM cross-section image taken at the edge of the crater. The depth of the crater was found to be ~15–20 nm by measuring the thickness of the remaining Ru inside the crater and subtracting it from the initial 50 nm thickness.

We compare the results of the optical laser damage experiment described above with three other single-shot damage experiments previously performed at XFEL facilities, where light with different photon energies was used. Identical samples were irradiated, namely 50 nm thick Ru films on Si substrates prepared with magnetron sputtering.

In the first experiment performed at the Free-electron LASer in Hamburg (FLASH [35]), femtosecond XUV pulses with 92 eV photon

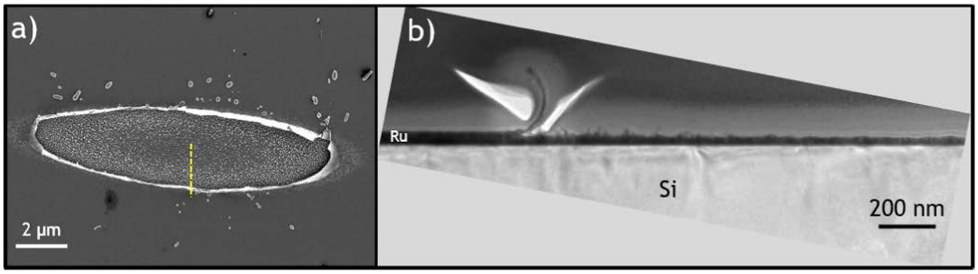

Fig. 2. (a) SEM image of Ru damage crater produced by a 100 fs 92 eV (13.5 nm) laser pulse with an incident peak fluence $F = 300$ mJ/cm^2. The yellow line indicates where the TEM cross-section is made. (b) TEM cross-section image taken along the short axis at the edge of the damage crater, illustrating ablation of the top 18–22 nm of Ru. (For interpretation of the references to colour in this figure legend, the reader is referred to the web version of this article.)

energy (13.5 nm wavelength) were used [23]. Exposures were performed in a high-vacuum chamber at grazing incidence conditions (20° grazing angle) mimicking the operation conditions for Ru thin film as an X-ray reflective mirror. The details of the experiment can be found in Refs. [12,23]. A SEM image of a typical damage crater produced in this experiment is shown in Fig. 2(a). The crater is similar to the one obtained after irradiation with the optical laser (see Fig. 1). Similar ablation of the top Ru layer is observed (see TEM image at the edge of the crater shown in Fig. 2(b)). The crater depth is measured in the same way as described above and is about 18–22 nm. We observe similar surface morphology inside the crater for optical and XUV cases: the roughness decreases from the edge towards the center of the crater.

Two other experiments, reported by Aquila et al. [21,24], were performed at SPring-8 Angstrom Compact free electron LAser (SACLA [36]). Ru films were exposed to single-shot femtosecond XFEL pulses with 7 and 12 keV photon energy (0.177 and 0.103 nm wavelength, respectively). Due to the much higher photon energy compared to the experiments described above, extremely grazing incidence conditions (0.26° and 0.17°, respectively) were applied to guarantee high reflectivity of Ru. The SEM and TEM images of the damage crater for the 7 keV case, together with the TEM image of the 12 keV crater are shown in Fig. 3. The craters are strongly elongated in one direction due to the extremely grazing AOI. Only a part of the crater is shown in Fig. 3(a). Similar to the experiments described above, ablation of the top Ru layer is observed for both the 7 and the 12 keV cases, with the reported value of the crater depth to be 10–20 nm. The bottom of the craters for the 7 and 12 keV exposures are considerably smoother, compared to the optical and XUV cases. Cracks inside the crater are observed on the SEM image, and the ones that spread through the entire Ru layer in the center of the crater are detected on the TEM images.

In all the described experiments, single-shot ablation thresholds were determined with the Liu method [37]. Crater areas were measured using optical microscopy. The spatial shape of the beam at XFEL facilities is typically non-Gaussian. For that reason, in XUV and hard X-ray experiments a fluence scan method [38,39] was used to characterize the spatial beam shape and effective beam area prior to the damage experiments.

Table 1
Summary of experimental conditions to determine single-shot ablation thresholds at four different photon energies: 1.5, 92, 7000 and 12000 eV. The threshold value F^{th} and crater depth are measured in the present work for the 1.5 eV case, while for the XUV (92 eV) and hard X-ray (7 and 12 keV) cases the values are taken from Refs. [23,21], respectively. The absorbed threshold fluence F^{th}_{abs} is calculated taking into account the surface reflectivity, R, and the fraction of energy that escapes from Ru due to electron emission, ξ. The latter is determined in the XCASCADE(3D) simulations.

Photon energy [eV]	1.5	92	7000	12000
Environment	atmosphere	high vacuum		
AOI[a], θ [deg]	~80	20	0.26	0.17
Photon penetration depth, δ [nm]	12.8	3.5	1.8	1.9
Surface reflectivity, R [%]	67	68	89.9	95
Pulse duration (FWHM), τ_p [fs]	90	100	20	20
Exp. dam. threshold, F^{th} [mJ/cm^2]	367 ± 66	200 ± 40	1395	14100
Fraction of escaped energy[b], ξ [%]	0	9	47	48
$F^{th}_{abs} = F^{th}(1-R)(1-\xi)$ [mJ/cm^2]	121 ± 22	58 ± 12	75	367
Abs. dose, $D = F^{th}_{abs}/\delta$ [eV/atom]	8	14	35	162
Exp. crater depth [nm]	15–20	18–22	10–20	15–20

[a] Measured from the sample surface.
[b] Calculated with XCASCADE(3D).

Table 1 summarizes the main results and parameters of the described experiments. Note that the threshold fluences reported in [21] should be scaled by a $sin(\theta)$ factor, in order to obtain the incident threshold fluence at the sample surface, F^{th}, where θ is the AOI measured from the sample surface. For better comparison of all four experiments, the single-shot ablation threshold values, F^{th}, are recalculated into the absorbed fluence $F^{th}_{abs} = F^{th}(1-R)(1-\xi)$ taking into account surface reflectivity, R, and the fraction of energy that escapes from Ru due to electron emission from the front surface, ξ. The latter is determined by the XCASCADE(3D) simulations reported below. In our assumption of instant electron thermalization, the electron emission in the optical case can only occur due to the tail of the Fermi-Dirac distribution, which is exponentially small at our calculated electron temperatures.

It is known that the surface roughness can increase the X-ray absorption at extremely small grazing angles [40], but for our conditions

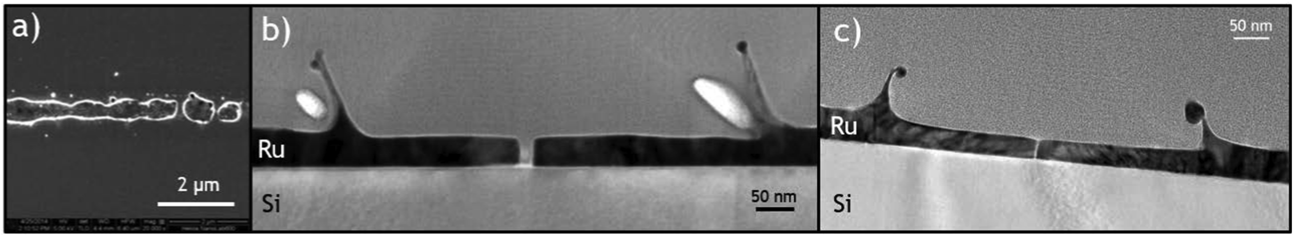

Fig. 3. (a) SEM image of Ru damage crater produced by a 20 fs 7 keV laser pulse near the ablation threshold fluence. (b) TEM cross-section image at the edge of the damage crater produced by the 20 fs 7 keV laser pulse, illustrating ablation of the top 10–20 nm of Ru. (c) TEM cross-section image at the edge of the damage crater produced by a 20 fs 12 keV laser pulse, illustrating ablation of the top 15–20 nm of Ru. All images are taken from Ref. [21,24].

such an effect on absorbed fluence is estimated to be insignificant.

An increase of the threshold fluence value with increasing photon energy is observed, although the case of 1.5 eV deviates from that trend, having a higher threshold value compared to 92 and 7000 eV, see Table 1. The deviation of the 1.5 eV case can be explained by a larger penetration depth of the optical light compared to XUV and hard X-rays at the considered experimental conditions (12.8 nm vs 3.5 and 1.8 nm, respectively). But different photon penetration depth alone cannot explain the full trend in the ablation threshold behavior. Moreover, the opposite trend could have been expected, since the photon penetration depth is the smallest for hard X-rays at our conditions. It is known from the literature [21,41,42] that X-ray photons are capable of creating significant electron cascades that can influence the absorbed energy distribution in the irradiated target and, hence, the damage processes. The effect of such electron cascading should be included in the analysis of X-ray matter interaction, especially in the high fluence regime. It becomes clear, if one calculates the absorbed dose without taking the transport of non-equilibrium electrons into account (see Table 1 and Ref. [21]). Another interesting observation is that despite orders of magnitude difference in the incident photon energy, all examined damage spots exhibit comparable crater depth, which indicates that the mechanisms responsible for damage may be similar.

The main goal of the present work is to study the effect of electron cascades created by photons with different energy on single-shot ablation in Ru films. To better understand the experimental results presented above, we perform simulations of laser pulse interaction with Ru at different irradiation conditions using our combined Monte Carlo-hydrodynamics approach that is described in the next section. With our simulations we aim to explain the similarities in the observed damage for considerably different irradiation conditions.

3. Model

The photoabsorption and non-equilibrium electron kinetics induced by incident photons are simulated with the classical Monte-Carlo (MC) code XCASCADE(3D) [28]. Cascading electrons with kinetic energy below a certain threshold (equal to the outermost ionization potential of the target atom, which is 8.12 eV for Ru) are considered as thermalized and provide a heat source for the 2T-HD model [27]. This model takes into account thermal diffusion of thermalized (equilibrium) electrons into the depth (in 1d) of the irradiated material, energy transfer from electronic into the ionic system and hydrodynamic evolution of the material due to thermo-induced stresses. As a result of such simulations, internal energy and temperature of both electrons and ions together with density, pressure and mass velocity can be obtained as functions of the depth and time.

In case of visible light, the energy of incident photons is not sufficient to induce electron cascades. For that reason, a standard heat source in the form of a temporally Gaussian laser pulse with exponential decay of the absorbed energy in depth is used as a heat source for the 2T-HD instead of the output of the XCASCADE(3D) code.

3.1. XCASCADE(3D)

The XCASCADE(3D) is an asymptotic trajectory event-by-event classical MC code that models X-ray-induced non-equilibrium electron transport in a target within the atomic approximation [28]. The target is represented as an infinite homogeneous arrangement of atoms with a density corresponding to the chosen material. The photoabsorption cross sections, parameters for the electron scattering cross sections and the ionization potentials of the target taken from the EPICS2017 databases [43] are also described in the atomic approximation.

The code accounts for the following processes: photoabsorption by core-shell levels, Auger recombination of created holes with release of Auger electrons, propagation of photo- and secondary electrons, and inelastic and elastic scattering of electrons on neutral atoms. All photo- as well as secondary electrons are traced until their energy falls below the predefined cutoff energy. Electrons with energies below this cutoff, as well as holes created in the valence atomic levels, are considered as thermalized. Their energy is treated as the energy of the conduction band electrons, forming a time- and space-dependent source term for further 2T-HD simulations as described below.

The inelastic scattering resulting in impact ionization is modeled with the binary-encounter-Bethe (BEB) cross sections [44], whereas for the elastic scattering, the Mott's cross section with the modified Moliere screening parameter is employed [45], both valid within the atomic approximation. The anisotropic scheme of electron-atom scattering is used [28].

The XCASCADE(3D) simulations are performed in two steps: first, we simulate a bulk material assuming all photons are absorbed at $z = 0$ ("surface"). Then, the realistic absorption profiles are taken into account by applying a convolution with the Lambert-Beer's law with the characteristic penetration depth, which depends on the target density, photon energy and the angle of incidence. This approach, previously utilized in [23,46], also enables one to estimate the total energy emitted from the sample by escaping electrons, but not the actual distribution of the energy above the surface.

In all experiments described above the authors used p-polarized light. In case of very small grazing incidence angles (7 and 12 keV), the polarization vector then is almost perpendicularly to Ru surface. We take the effect of polarization into account by allowing photoelectrons to travel only perpendicular to the surface (up and down) until their first scattering event. For simplicity, we use the same approximation for 92 eV photons, although the AOI is no longer small. It was shown that for 92 eV the effect of polarization is negligible due to small cascade ranges and quick randomization of the electron motion [46].

The applicability of the XCASCADE(3D) code is limited to the fluence regime when the density of cascading electrons is considerably lower than the atomic density. In that case the electron-atom scattering is dominant, while electron-electron interaction can be neglected. We checked that this condition was fulfilled in all the simulations presented in this work.

This limitation also allows to always use the cross sections of unmodified, unexcited material. As we show below, the cascade duration in Ru is short at the considered irradiation conditions. The material properties that can influence the cascading process do not change significantly during this time due to the excitation of the target. That justifies the application of the XCASCADE(3D) code to model the cascading process in Ru for fluences at which damage is expected on later timescale. In terms of incident photon energy, the code is applicable in a wide range from ~50 eV up to a few tens of keV.

An *a posteriori* analysis of our results suggests that during the cascading time (few tens of fs), the irradiated material properties used in the XCASCADE(3D) simulations do not significantly change. That justifies a coupling between XCASCADE(3D) and 2T-HD using a scheme without feedback, when the output data from MC simulations are passed one-way into the 2T-HD model as the input.

3.2. Two-temperature hydrodynamics and equation of state

The energy distribution of thermalized conduction band electrons, $U(z, t)$, obtained with the XCASCADE(3D) calculations is used to form a heat source in the 2T-HD model [27]. The 2T-HD equations in Lagrangian mass coordinates take the following form:

$$\frac{\partial}{\partial t}\left(\frac{1}{\rho}\right) = \frac{\partial u}{\partial m}, \tag{1}$$

$$\frac{\partial u}{\partial t} + \frac{\partial P}{\partial m} = 0, \tag{2}$$

$$\frac{\partial \varepsilon_e}{\partial t} + P_e\frac{\partial u}{\partial m} = \frac{\partial}{\partial m}\left(\kappa\rho\frac{\partial T_e}{\partial m}\right) - \frac{\alpha}{\rho}(T_e - T_i) + S, \tag{3}$$

$$\frac{\partial \varepsilon_i}{\partial t} + P_i\frac{\partial u}{\partial m} = \frac{\alpha}{\rho}(T_e - T_i). \tag{4}$$

Here m is Lagrangian mass coordinate:

$$dm = \rho dz, \quad m = \int_{z_0}^{z} \rho dz, \tag{5}$$

$\rho(z, t)$ is the material density, z is the depth Cartesian variable, z_0 is the Cartesian coordinate of the material surface and $u = dz/dt$ is the velocity of a Lagrangian particle. Eqs. (1) and (2) represent the conservation of mass and momentum, respectively. The conservation of energy is written separately for electronic and ionic subsystems, accounting for energy exchange between them, Eqs. (3) and (4), respectively. Such a separation is valid in the two-temperature (2T) approximation, when $T_e \neq T_i$, with T_e and T_i being electron and ion temperatures, respectively. The specific internal energies per unit mass of the electronic and ionic subsystems are ε_e and ε_i, respectively.

The energy exchange between electrons and ions is governed by the term $(\alpha/\rho)(T_e - T_i)$, where $\alpha = \alpha(T_e)$ is the electron temperature dependent electron-phonon coupling factor. The heat diffusion is assumed to be in the Fourier form defined by the heat flux $\kappa\rho(\partial T_e/\partial m)$, where $\kappa = \kappa(\rho, T_e, T_i)$ is the density and temperature dependent electron thermal conductivity. The terms $P_e(\partial u/\partial m)$ and $P_i(\partial u/\partial m)$ in the energy conservation law equations define the work performed by electronic and ionic subsystems, respectively.

The heat source $S(z, t)$ is obtained from the XCASCADE(3D) calculations as the time derivative of the energy density of thermalized electrons:

$$S(z, t) = \frac{\partial U(z, t)}{\partial t}. \tag{6}$$

In the case of optical excitation, where there is no cascading effect, we use the standard heat source, representing heating of the electronic system with a temporally Gaussian laser pulse with exponential decay of absorbed energy in depth:

$$S(z, t) = \sqrt{\frac{4\ln 2}{\pi}}\frac{F_{abs}}{\delta\tau_p\rho}\exp(-4\ln 2(t/\tau_p)^2)\exp\left(-\frac{z(m, t) - z(m_0, t)}{\delta}\right), \tag{7}$$

where F_{abs} is the absorbed fluence, δ is the photon penetration depth, τ_p is the laser pulse duration, $z(m, t)$ is the trajectory of a Lagrangian particle with a coordinate m and m_0 is the Lagrangian coordinate of the irradiated target surface.

The system of Eqs. (1)–(4) has to be completed with the equations of state (EOS), which describe pressure and internal energy of the material as functions of density, electron and ion temperatures. These equations govern the thermodynamics of the material in the two- and one-temperature states. The physics of the 2T states of metals is studied in detail [47–50]. However, for each particular metal the corresponding parameters are unique and must be obtained separately. In our separate work [29], the 2T EOS for single crystal hexagonal close-packed Ru are obtained and are applicable in a wide range of densities, temperatures and pressures that can be realized after irradiation of Ru with femtosecond high fluence laser pulses.

The idea of an analytical approximation of the 2T states of metals is to present the internal energy and pressure as a sum of electronic and ionic components [51]: $P = P_i + P_e$ and $\varepsilon = \varepsilon_i + \varepsilon_e$. In the framework of the Mie-Grüneisen approximation [51] the ionic components can be presented as a sum of cold and thermal parts. So for the total internal energy and pressure we have:

$$\varepsilon(\rho, T_e, T_i) = \varepsilon_i^{cold}(\rho) + \varepsilon_i^{T}(T_i) + \varepsilon_e(\rho, T_e), \tag{8}$$

$$P(\rho, T_e, T_i) = P_i^{cold}(\rho) + P_i^{T}(\rho, T_i) + P_e(\rho, T_e). \tag{9}$$

The procedures of obtaining analytical approximations for each term in Eqs. (8) and (9) is described in [29]. Calculations of the electron-phonon coupling factor $\alpha(T_e)$ and the electron thermal conductivity $\kappa(\rho, T_e, T_i)$ are also described in [29].

The system of Eqs. (1)–(4) completed with the EOS (9) and (8) is solved using the implicit finite-difference method. The artificial viscosity is introduced to suppress non-physical oscillations in the obtained solutions [52].

4. Results

In this section we present the results of the simulations with our combined approach in two fluence regimes. First, a relatively low fluence is applied in order to stay below the melting point in simulations for all four photon energies. In that regime we stay strictly within the applicability of the 2T-HD part of our model for Ru, which currently does not take into account the melting. A second set of simulations is performed in a high fluence regime corresponding to the ablation threshold values obtained in the experiments (see Table 1). In such a regime of high fluences, we expect melting of Ru to occur. The fact that melting is not simulated, due to the lack of knowledge of the EOS for liquid Ru, may influence the accuracy of our calculations. Therefore, we only aim to provide a qualitative analysis of the damage processes, which enables us to explain the trends observed in the experiment.

4.1. The fluence regime below melting

We perform simulations of a thick Ru target exposed to single femtosecond laser pulses with four photon energies: 1.5, 92, 7000 and 12000 eV. For a clean comparison, the thickness of the Ru layer in each simulation is chosen large enough to mimic a bulk sample and eliminate possible substrate effects. For the case of optical excitation (1.5 eV) we consider no electron cascading and assume instantaneous electron thermalization. We perform XCASCADE(3D) calculations only for the XUV (92 eV) and hard X-ray (7 and 12 keV) cases.

First, we study the effect of different incident photon energies on the cascading kinetics and the final distribution of the absorbed energy stored in low-energy (thermalized) conduction band electrons. For pure theoretical comparison, we set the irradiation conditions such that the total absorbed volumetric energy density is identical for all photon energies. To achieve that, we set the values of the absorbed fluence and photon penetration depth to be the same for all photon energies. The crucial difference will be in how the absorbed energy is transported into the depth of Ru by cascading electrons. The photon penetration depth in all the cases is chosen to be equal to the optical (1.5 eV) skin depth of Ru, $\delta = 12.8$ nm. We set the value of $F_{abs} = 20$ mJ/cm^2 in order to stay below melting in all four simulations, which guarantees the applicability of the whole model. The absorbed fluence is calculated taking into account the surface reflectivity, R, and a fraction of the energy that escapes from Ru due to electron emission, ξ: $F_{abs} = F(1 - R)(1 - \xi)$. Table 2 summarizes the irradiation parameters used in the simulations together with the most important results.

The values of ξ are extracted from XCASCADE(3D) calculations by integrating the energy distribution above the surface of Ru and are equal to 3, 38 and 44% for 92, 7000 and 12000 eV, respectively. Only a small portion of the energy carried by the cascading electrons is released from the surface in the 92 eV case due to the low energy of the particles. A minority of electrons is able to reach the surface and overcome the work function of Ru (4.71 eV [53]). Contrarily, a considerable part of the energy leaves the target in the case of hard X-rays due to the higher energy of the cascading electrons. The value is lower than 50%, since photoelectrons that travel up perpendicular to the surface before leaving the material can lose energy by creating secondary electrons. The value of ξ is higher for 12 keV, because the probability for a photoelectron to create a secondary electron while travelling from the point of photoabsorption to the surface is lower for higher energy of a photoelectron.

Table 2
Summary of irradiation conditions used in the simulations in the fluence regime below melting. Irradiation conditions are chosen to have equal volumetric absorbed energy density (dose), F_{abs}/δ, for all considered photon energies. Cascade durations are calculated for the 92, 7000 and 12000 eV cases. No cascading is considered for the 1.5 eV case.

Photon energy [eV]	1.5	92	7000	12000
Pulse duration (FWHM), τ_p [fs]	20			
AOI[a], θ [deg]	80	29.2	0.59	0.32
Photon penetration depth, δ [nm]	12.8			
Surface reflectivity, R [%]	67	14.6	20.6	53.2
Fraction of escaped energy, ξ [%]	0	3	38	44
Incident fluence, F [mJ/cm^2]	61	24	41	76
Absorbed fluence, $F_{abs} = F(1-R)(1-\xi)$ [mJ/cm^2]	20			
Cascade duration [fs]	–	0.2	4.4	9.9

[a] Measured from the sample surface.

In the calculations of ξ we do not take into account the surface charging effect, therefore the obtained values can be considered as the upper limit. The effect is expected to be insignificant for the considered irradiation conditions. For the 92 eV case, the electron emission is already negligible. For the hard X-ray cases a major part of the energy is escaping via photoelectrons with high kinetic energy, which should enable them to travel a sufficient distance from the sample surface without being attracted back.

The distribution of the absorbed energy density stored in low-energy (thermalized) electrons, $U(z, t)$, at the moment of time when the cascading is finished (defined as the time when density of cascading electrons decreases below 1% of its maximum value) is shown in Fig. 4 for 92, 7000 and 12000 eV photons. The top 50 nm of Ru are shown in Fig. 4(a), while Fig. 4(b) focuses on the deeper part of Ru with long energy tails in the 7 and 12 keV cases.

As discussed above, since the absolute majority of excited electrons in the optical irradiation case (1.5 eV) has energy below 8.12 eV cutoff, there is no cascading in such a case by our definition. Therefore, the absorbed energy density can be represented with the Lambert-Beer's law as $(F_{abs}/\delta)exp(-z/\delta)$. Photons with 92 eV energy are capable of ionizing 4s, 4p, 4d and 5s electrons in atomic Ru, with 4d and 5s valence levels representing the conduction band of the material in our atomic approximation, as we discussed in [23,46]. Photoelectrons with relatively low kinetic energy (~10–40 eV) are thus created, which results in a very short cascading range, since these electrons lose the energy below the cutoff after only a few collisions. Only a slightly deeper spread of the energy is observed for the 92 eV case compared to 1.5 eV, which demonstrates a small effect of electron cascading in Ru for 92 eV photons.

Photons with 7 and 12 keV energies are capable of ionizing core-shell electrons down to the 2s level of Ru, creating a majority of photoelectrons with energy of ~3800 and 8800 eV, respectively. Their cascading ranges are considerably larger than those in the XUV case. A much deeper spread of energy for hard X-rays, having the same total amount of absorbed energy, results in a much lower energy density in the near surface region compared to the XUV and optical cases, see Fig. 4(a). In Fig. 4(b), the peak at 170 nm depth on the 12 keV curve corresponds to the average photoelectron range for that photon energy. The peak is separated from the contribution of secondary electrons which have lower energy and, hence, travel a shorter distance. For the 7 keV curve, the contributions from photo- and secondary electrons happen to be mostly overlapping, therefore no separate photoelectron peak is observed.

An average single (produced by one photon) cascade duration is determined as the FWHM of the energy density time derivative [54]. The results are 0.2, 4.4 and 9.9 fs for 92, 7000 and 12000 eV, respectively. Such extremely short times justify our approximation that during the cascading, the material is considered as undamaged within the MC scheme.

The 2T-HD calculations are performed using the power densities $\partial U(z, t)/\partial t$ as heat sources. For 1.5 eV the standard heat source, Eq. (7), is used. Fig. 5 shows the time dependence of electron and ion surface temperatures. All four cases exhibit thermal non-equilibrium between electrons and ions during the first ~1–2 ps. Although the qualitative behavior of the surface temperatures is similar for all photon energies, the reached temperatures differ considerably. The higher the photon energy, the deeper electrons transfer an equal amount of absorbed energy (cf. Fig. 4), which results in a lower surface temperature. Note, that T_i stays below the melting temperature $T_m = 2607$ K in all the calculations.

The depth profiles of ion temperature T_i and total pressure P at $t = 5$ ps for different photon energies are shown in Fig. 6(a) and (b), respectively. The time $t = 5$ ps is chosen as the time when the tensile pressure wave is already formed and reached an amplitude close to the maximum value (see description below). A much deeper distribution of absorbed energy by cascading electrons for the 7 and 12 keV cases results in a more gradual change of ion temperature with depth compared to a steep decrease in the cases of 1.5 and 92 eV photons. The small peak in the ion temperature profiles at the depth of ~10 nm is due to the compression of material in that region.

Ultrafast almost isochoric heating of a target by a femtosecond laser pulse results in generation of thermo-induced stress. Such a situation is

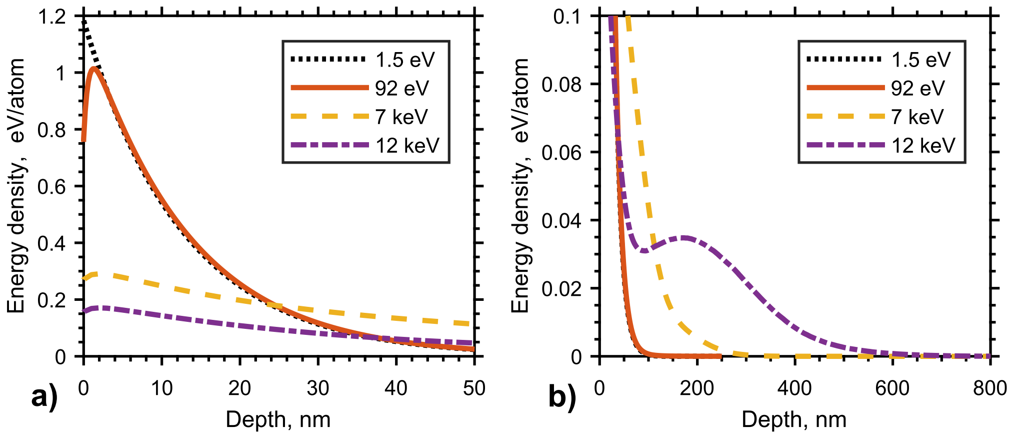

Fig. 4. (a) Distribution of energy density $U(z, t)$ in the top 50 nm of irradiated Ru at the end of the cascading process, calculated with the XCASCADE(3D) code for different photon energies in the fluence regime below melting. The irradiation parameters are listed in Table 2. Since there is no cascading in the 1.5 eV case, the distribution of energy is represented with the Lambert–Beer's law (dotted line). (b) The same distribution shown in the entire Ru to emphasize the long energy tails in 7 and 12 keV cases.

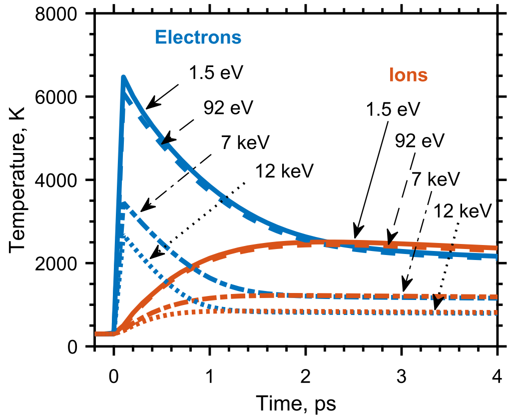

Fig. 5. Time dependence of electron and ion surface temperatures, calculated with the 2T-HD code for different photon energies in the fluence regime below melting. The irradiation parameters are listed in Table 2.

referred to as the stress confinement regime [23,26,55] and is realized when the heating time is shorter than the acoustic relaxation time. The latter can be determined as the heated depth divided by the speed of sound. For Ru at the considered irradiation conditions the acoustic time is ~10 ps, while the heating time is ~1 ps (see Fig. 5). Therefore, the material is in the stress confinement regime.

The compressive wave created at the surface propagates into the depth of the irradiated material and is followed by the tensile wave, Fig. 6(b), due to the existence of a free surface. The fracture typically occurs when the amplitude of a tensile wave overcomes the spall strength of the material [26]. The spall strength of Ru at ultra-high strain rates of about $10^{10}\ \mathrm{s}^{-1}$ that are typically realized during the ablation process is unknown. For solid iron the spall strength at $10^{9}\ \mathrm{s}^{-1}$ strain rate is 15 GPa [56]. The spall strength of Ru must be even higher, judging from the comparison of cold curves for these two metals (a cold curve, which is the dependence of pressure on volume/density at absolute zero temperature, can be extracted from [57]). In the studied cases, the tensile pressure in Ru stays above -7 GPa, therefore no fracture of material is expected.

The general behavior of pressure profiles in Fig. 6(b) is similar for all photon energies, but the amplitudes of the pressure waves are considerably different. Stronger temperature gradients in the cases of 1.5 and 92 eV result in stronger pressures compared to the 7 and 12 keV case.

The performed analysis demonstrates that the electron cascading effect in the 7 and 12 keV cases plays an essential role in the distribution of the absorbed energy in Ru, making the hard X-ray cases considerably different from the 1.5 and 92 eV cases. Despite the fact that the energy is transferred much deeper for 7 and 12 keV, which results into a lower energy distribution in the top 50 nm of Ru, there are still temperature gradients that induce pressure waves. The amplitudes of those pressure waves are much smaller than in the 1.5 and 92 eV cases. Based on our analysis, one can expect higher amplitudes of pressure waves for higher fluences, which can result into damage. We investigate the evolution of the Ru target irradiated with fluences corresponding to the measured damage threshold values in more details in the next section.

4.2. *The fluence regime at the ablation threshold level*

In this section we perform similar simulations as the ones described above, but for the irradiation conditions used in the experiments (see Table 1). The absorbed fluences are chosen to be 121, 58, 75 and 367 mJ/cm^2 for 1.5, 92, 7000 and 12000 eV photon energy, respectively, which correspond to the measured single-shot ablation thresholds, F_{abs}^{th}. The values of ξ calculated for the irradiation conditions considered here are 9, 47 and 48% in the 92, 7000 and 12000 eV cases, respectively. The values are higher, compared to the ones reported in the previous section, because the photon penetration depth is now smaller (see Table 1).

To significantly simplify the simulation, all calculations are again performed for the thick Ru sample, with a thicknesses large enough to mimic bulk material for each particular photon energy, whereas the thin Ru films with a thickness of 50 nm on Si substrates were used in the experiment. It will be shown below that the prime mechanism of damage with the fluences near the ablation threshold does not involve a major role of the substrate. The fact that the crater depth measured in all considered experiments is smaller than half of the film thickness also supports that assumption (see Discussion).

Fig. 7 shows the distribution of the absorbed energy density at the end of the cascading process for 92, 7000 and 12000 eV. Again, the exponential decay of the absorbed energy for the optical case corresponds to the Lambert-Beer's law with the photon penetration depth $\delta = 12.8$ nm. Fig. 7(a) shows the distribution of the energy in the top 50 nm of Ru, while Fig. 7(b) shows the depth up to 700 nm focusing on the long energy tails for the 7 and 12 keV cases. The dose of several eV/atom is achieved at the near surface region in all four simulations. Such doses are considerably higher than that required for melting of Ru (~1 eV/atom, see Fig. 4(a) and Ref. [58]). This indicates that stronger damage is expected, which is confirmed in the experiments. Similar energy density distributions in the top 50 nm are observed in Fig. 7(a) for the cases of 1.5, 92 and 12000 eV, while the 7000 eV curve lies considerably lower. We will discuss the distinction of the 7 keV case

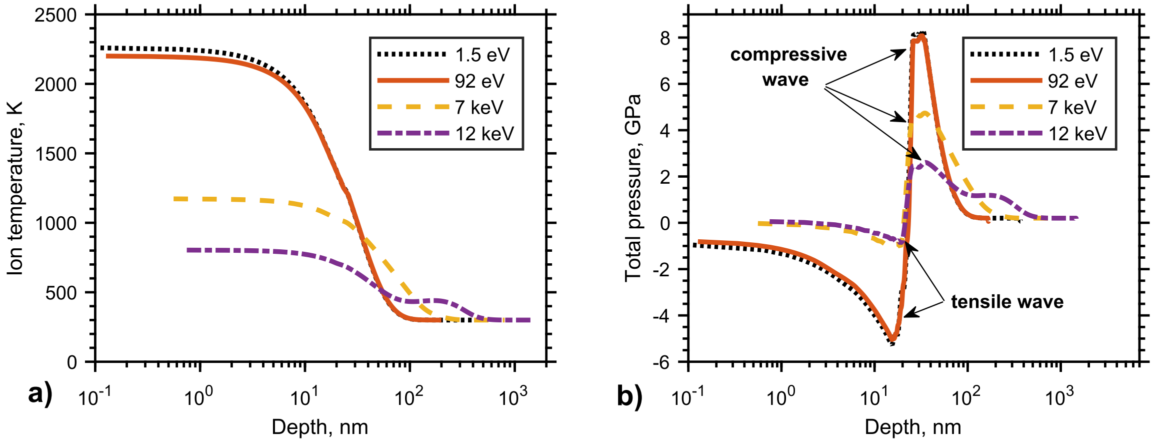

Fig. 6. (a) Ion temperature and (b) total pressure depth profiles at $t = 5$ ps, calculated with 2T-HD code for different photon energies in the fluence regime below melting. The irradiation parameters are listed in Table 2.

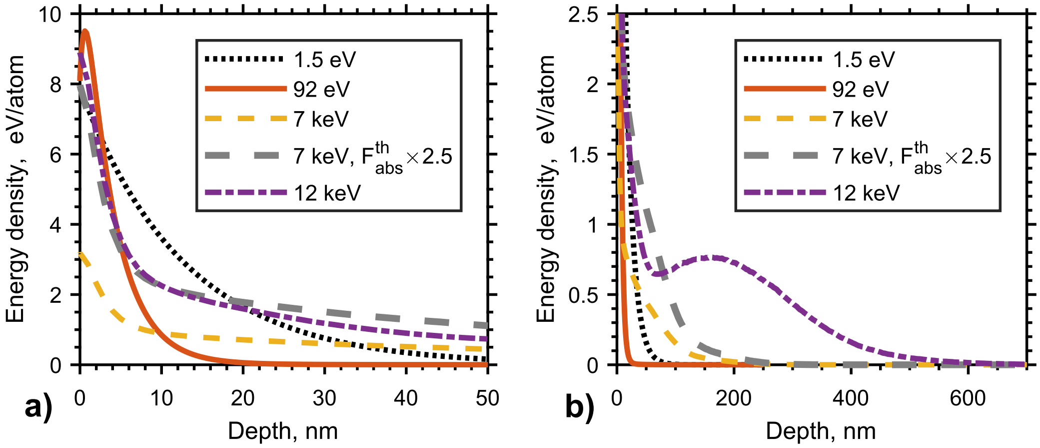

Fig. 7. (a) Distribution of energy density $U(z, t)$ in the top 50 nm of irradiated Ru at the end of the cascading process, calculated with the XCASCADE(3D) code for different photon energies in the fluence regime corresponding to the measured ablation threshold. The irradiation parameters are listed in Table 1. Since there is no cascading in the 1.5 eV case, the distribution of energy is represented with the Lambert–Beer's law (dotted line). The thick dashed grey line shows the 7 keV case calculated with a fluence 2.5 times higher than the measured ablation threshold. The fluence has to be increased in order to achieve a similar distribution of energy density in the top 50 nm for all considered photon energies (see discussion in the text). (b) The same distribution shown in the entire Ru to emphasize the long energy tails in 7 and 12 keV cases.

below.

The long range behavior, Fig. 7 (b), is different for the cases of 92, 7000 and 12000 eV photons due to different impact of the cascading effect: cascading electrons propagate deeper for higher photon energy as discussed above. Let us recall that calculations are performed for thick Ru, while according to the experiment the region $z > 50$ nm should correspond to the Si substrate. The electron range in Si is approximately 4.5 and 5.5 times larger than in Ru for the incident photon energy of 7 and 12 keV, respectively. Based on that rough estimation, the tails of the energy distribution, Fig. 7(a), should be stretched in the region $z > 50$ nm with corresponding factors (not shown here), which will result in the dose in that region being lower than 0.25 eV/atom. Such dose is considerably lower than the melting dose for Si, ~0.65 eV/atom [59,60], which guaranties that the Si substrate is not damaged at the given irradiation conditions. This conclusion is also supported by the experimental evidence of no visible damage in the substrate.

Similar to Fig. 4, the peak at 160 nm in the 12 keV case in Fig. 7 is due to photoelectrons, while the near surface peak is the contribution from secondary electrons. More specifically, the peak-like distribution of energy in the top 10 nm of Ru for all three photon energies (92, 7000 and 12000 eV) is caused by Auger electrons produced during many-step decay of core-shell holes created after release of a photoelectron. The average kinetic energy of such Auger electrons is relatively small, so they do not travel far and stay in the near surface region. In the 92 eV case Auger electrons have higher energy than photoelectrons and make the dominant contribution to the energy distribution.

Similar energy distributions in the top part of Ru should induce similar hydrodynamic evolution and eventually lead to similar damage phenomena observed in the experiment (ablation of the top 10–20 nm). The long range energy tails in the spatial energy distribution are not expected to play a major role at our fluences, apart from being the energy sink from the near surface region. The temperature gradients are low in the deeper region compared to those in the top 20 nm of Ru. Hence, no strong pressure waves are generated there. The tails therefore act as an almost uniform mild heating source for the deep parts of the sample. That can potentially influence later stages of material evolution, playing a role in the recrystallization process and the formation of the final structure that is observed post mortem in the experiment.

According to our hypothesis that the distribution of the absorbed energy in the near surface region of Ru plays the dominant role in the ablation process detected in the experiment, one should expect similar energy profiles in that region for all considered photon energies. However our calculations show that the 7 keV profile differs from the others at the considered experimental conditions (see Fig. 7(a), thin dashed line). Only if we increase the fluence by 2.5 times, the profile becomes very similar to the other ones (thick dashed line).

We justify the need of introducing a fluence correction factor with the following argument. Sophisticated geometry conditions in the reported experiment for 7 and 12 keV cases [21], namely the extremely grazing AOI, makes the procedure of accurate determination of the damage threshold values very challenging. The complicated shape of the damaged craters (very stretched thin lines of about $100 \times 1\ \mu$m size [21]) may introduce additional large errors into the procedure of measuring the area of such craters, and consequently into the damage threshold values.

To study how the cascading processes at different photon energies influence the hydrodynamic evolution of Ru, we perform 2T-HD calculations with heat sources obtained with the XCASCADE(3D) simulations (except for the optical case in which Eq. (7) is used). In the case of 7 keV we show results obtained with the fluence 2.5 times higher than the measured ablation threshold.

The ion temperature evolution in Ru during the first 8 ps is shown in Fig. 8 for 1.5, 92, 7000 and 12000 eV photon energies. As one can see, all four cases exhibit strong heating of the ions near the surface considerably above the melting temperature of Ru, $T_m = 2607$ K. The peaks on the ion temperature profiles that propagate into the depth of the sample with time are, as already mentioned above, due to strong compression of the material in that region (see pressure profiles below). Most of the heat is confined in the top 20–40 nm of Ru in the cases of 1.5 and 92 eV. For 7 and 12 keV the heat is spread over a larger region in accordance with the energy profiles shown in Fig. 7.

The maximum depth of melting during the considered 8 ps timescale is estimated to be 30, 12, 57 and 42 nm for 1.5, 92, 7000 and 12000 eV, respectively. These values are obtained by comparing the temperature profiles with the value $T_m + T_h$, where $T_h = H_m/C_i = 746$ K. Here $H_m = 4.7\cdot10^9$ J/m^3 is the latent heat of melting and $C_i = 6.3\cdot10^6$J/m^3/K is the ion heat capacity at the melting temperature [61]. Note, that the melting depth in the 7 keV case would expand into the substrate in the experiments. However, as we mentioned earlier, the actual absorbed dose in the substrate is much lower due to a large spread of the photoelectrons, therefore no melting is actually expected at those depths.

The corresponding total pressure profiles are shown in Fig. 9. Strong compression waves with maximum amplitudes of ~40–50 GPa are

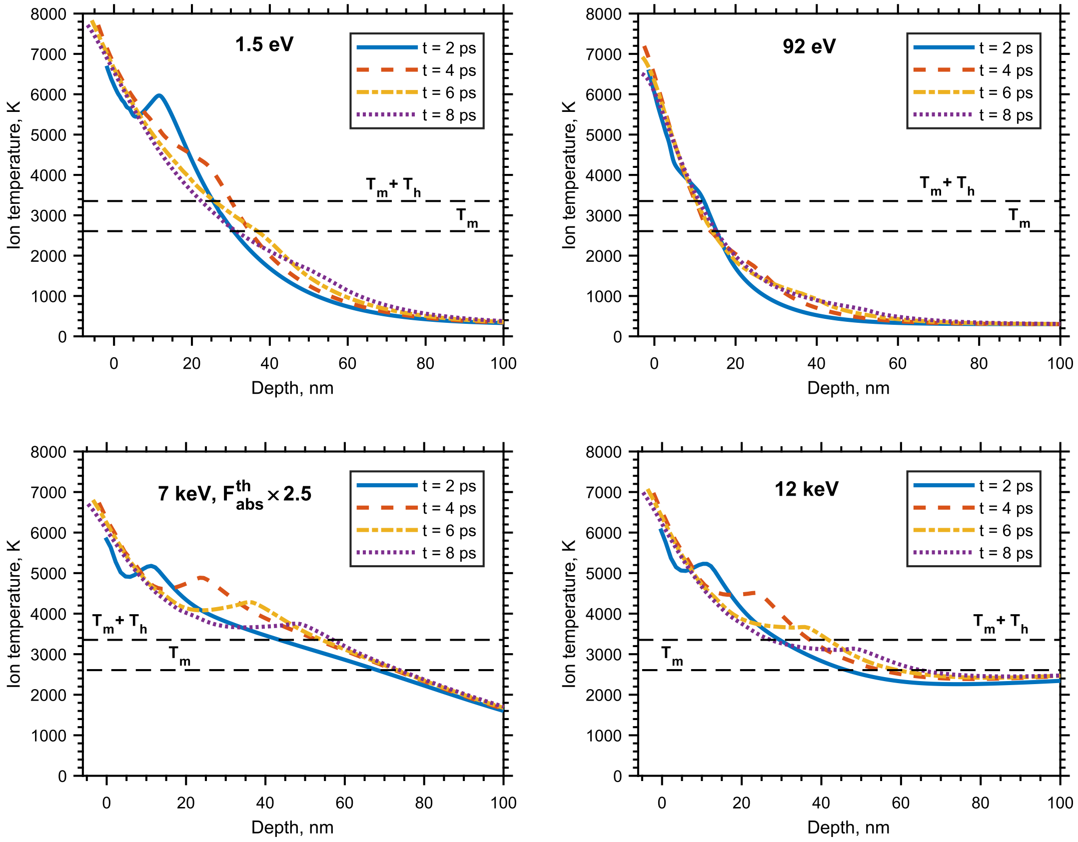

Fig. 8. Ion temperature depth profiles evolution in Ru calculated with the 2T-HD code for different photon energies and fluences corresponding to the measured ablation thresholds. The values of the absorbed fluence (with surface reflectivity and energy escape from the sample via energetic electrons taken into account) are 120, 55, 185 and 364 mJ/cm^2 for the 1.5, 92, 7000 and 12000 eV photons, respectively. Other irradiation parameters are listed in Table 1. Note that for 7 keV we show the results of calculations with 2.5 times higher fluence than the measured ablation threshold. The black dashed lines show the melting temperature of Ru $T_m = 2607$ K and the value $T_m + T_h = 3353$ K, where the latent heat of melting is taken into account.

followed by rarefaction tensile waves. For accurate analysis of the strength of the tensile wave in the context of damage, one needs to know the spall strength of liquid Ru at high strain rates of ~10^{10} s^{-1} that are realized during the ablation processes. Unfortunately, very limited data on spall strength of metallic melts are available in the literature [62–65], with Ru not being studied at all in this respect. Due to that reason we use the experimental knowledge of the crater depth (10–20 nm) as an indication where the fracture of the material occurs. The maximum amplitude of the tensile wave reached at the depth of 10–20 nm lies in the range of 10–15 GPa for all photon energies. These values can be considered as our model prediction of the spall strength of Ru at high strain rates. For comparison, the spall strength of solid iron at 10^9 s^{-1} strain rate is 15 GPa [56]; the spall strength of liquid aluminum at ~10^9 s^{-1} strain rate is 3.2 GPa at $T = 1100$ K and is decreasing with temperature [64].

Similar amplitudes of the tensile pressure reached in the top 20 nm region for all photon energies explain the observed similarities in the crater depths.

5. Discussion

5.1. Physical reasons for energy confinement

A comparison of ablation craters in Ru obtained in the experiments demonstrates that at threshold fluences damage occurs in the top 10–20 nm for all considered irradiation conditions. Our theoretical analysis shows a similar distribution of the absorbed energy after the cascading process in the top 10–20 nm of Ru for all four photon energies, if for the 7 keV case one increases the absorbed fluence by a factor of 2.5. A similar energy distribution in the top 20 nm induces a similar hydrodynamical evolution and, hence, similar ablation craters.

Separate XCASCADE(3D) calculations show that for hard X-rays (7 and 12 keV), the peaks in the local energy density in the top 10 nm, see Fig. 7(a), are primarily caused by the Auger electrons created at the positions of the photoabsorption due to many-step decays of core–shell holes. For both considered hard X-ray energies, the electron ranges of those Auger electrons are around 8 nm, leading to the accumulation of the energy in a small volume and resulting in damage. This number is calculated taking into account the spectrum of Auger electrons created by the incoming X-ray photon and their corresponding electron ranges, all obtained using the XCASCADE(3D) code. It has also been independently verified using the Auger spectra from the *ab initio* code XATOM [66–68], based on the Hartree-Fock-Slater approximation. Although such electrons possess less than half of the absorbed energy and the rest is brought deeper by the energetic photoelectrons, the latter spread the energy over a larger volume, thus decreasing the effective local absorbed dose in the depth. Only in the vicinity of the surface the energy density is sufficient to cause damage under our conditions.

This simulation result can be understood by considering the involved cross sections. First of all, the probability for a hard X-ray photon to create a core-shell hole is more than 100 times higher than that to create a valence hole [43]. It means that absorbed photons predominantly initiate Auger cascades at the positions of their absorption. Auger electrons have relatively low kinetic energies, which confines them to the proximity of their creation - the photoabsorption site. In contrast, the photoelectrons on their paths predominantly excite valence electrons. Only very few core–shell holes are created by the cascading electrons [43]. The corresponding energy loss of the

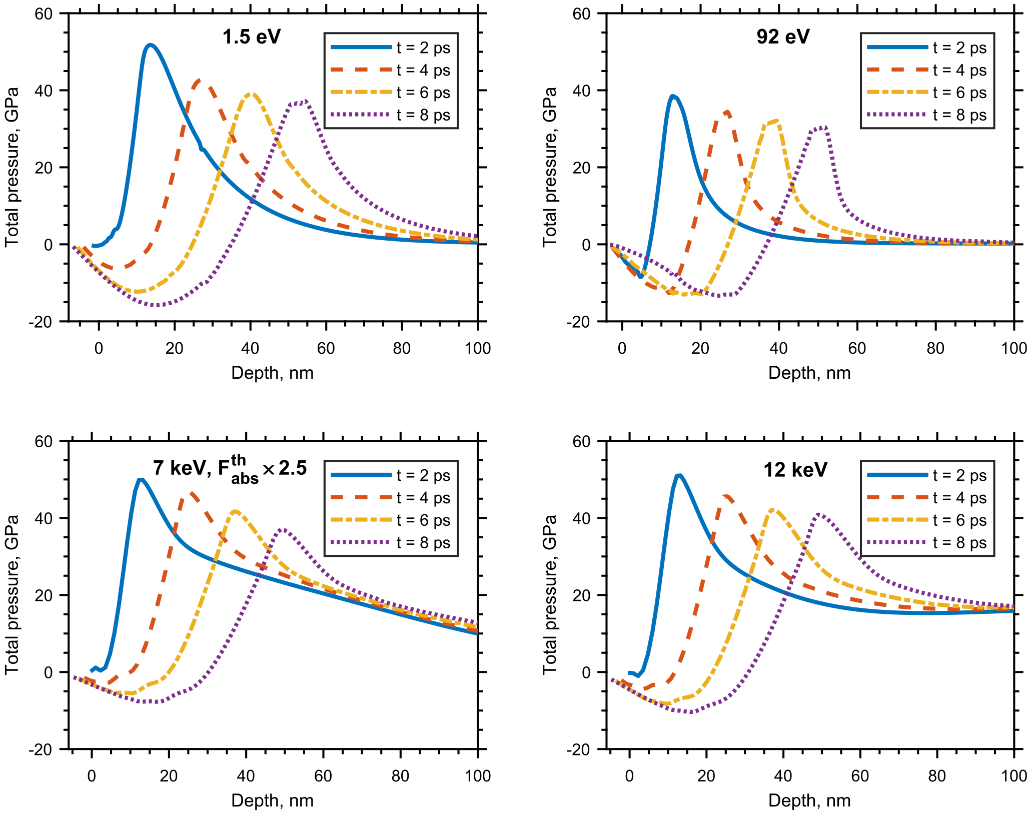

Fig. 9. Total pressure depth profiles evolution in Ru calculated with the 2T-HD code for different photon energies and fluences corresponding to the measured ablation threshold. The values of the absorbed fluence (with surface reflectivity and energy escape from the sample via energetic electrons taken into account) are 120, 55, 185 and 364 mJ/cm^2 for the 1.5, 92, 7000 and 12000 eV photons, respectively. Other irradiation parameters are listed in Table 1. Note that for 7 keV we show the results of calculations with 2.5 times higher fluence than the measured ablation threshold.

photoelectrons is around 10 eV/nm, thus the photoelectrons typically spread the energy over a large depth.

The fact that Auger electrons may play a role in bulk materials evolution after irradiation with X-rays was discussed in [69]. An importance of Auger electrons was shown for small clusters irradiated with X-rays [70]. Since energetic photoelectrons can leave a cluster thus bringing out most of the absorbed energy from it, the remaining Auger electrons and Coulomb repulsion lead to the subsequent damage. However, for our case of metals, no Coulomb repulsion is expected and therefore one can see the pure effect of Auger electrons. To our knowledge, no corresponding studies have been published for bulk solids.

In case of 92 eV photons the photoabsorption also mostly results in the creation of the core-shell holes, which however possess a major part of the photon energy. The corresponding Auger cascades thus, again, become the main cause of the eventual damage.

For the low energy photons the localization of absorbed energy in the vicinity of the surface always occurs due to the absence of energetic electrons. For the high energy photons the localization of energy is due to the Auger electrons. Therefore, a similar spatial energy distribution near the surface leads to a very similar hydrodynamical evolution of the target and eventual damage *independently of the photon energy*. We expect that such a mechanism is universal in a wide range of photon energies and in various materials, however a rigorous verification is outside of the scope of this paper.

5.2. The 7 keV case

Without the correction factor of 2.5 in the absorbed fluence, the maximum amplitude of the tensile pressure at the depth of 20 nm for the 7 keV case reaches only 5.7 GPa. This value is too low to expect damage and takes the 7 keV out of the trend when compared to other considered photon energies.

Another indication that the damage threshold for the 7 keV case has to be higher follows from the analysis of the damage threshold values for all considered cases (see Table 1). Simulation results presented in Fig. 4 show that the deeper penetration of the absorbed energy results in a lower energy density in the surface region. Therefore, one expects the damage threshold value to increase with increasing energy penetration depth. Then, as it follows from Fig. 7, the considered photon energies should be listed in the order of the threshold fluence increase in the following way: 92, 1.5, 7000 and 12000 eV. One can see from Table 1 that this is only possible if the threshold fluence for the 7 keV case is increased. A factor of 2.5 increase results in a reasonable trend.

We believe that the discrepancy between the experiment and our calculations for the 7 keV case can only be completely resolved with more experimental data.

5.3. Melting

The 2T EOS obtained in [29] do not take into account the phase transitions, i.e. are valid only for solid Ru. Construction of a wide range EOS (with different phases included) for Ru requires a separate dedicated study and is beyond the scope of the present work. Our 2T-HD calculations show that the top part of the sample is subjected to melting in all considered irradiation conditions (see Fig. 8). Melting can influence the pressure profiles in the molten region of the sample. It can be shown, for example, that for Au and Al the influence of melting is small if one compares the wide range EOS [71] with the solid phase EOS in the Mie-Grüneisen approximation [51] for these two metals. The Grüneisen parameter should be taken as 3.1 and 2.1 for Au and Al, respectively. With a separate classical molecular dynamics simulation [32,72–74] we checked that the effect of melting on the resulting pressure profiles during the first several ps is small for Ru as well (results will be reported elsewhere). Such a verification is obtained by comparing the pressure profile at t = 2 ps for the XUV case, calculated with molecular dynamics (melting is naturally included) and with the present 2T-HD code. The difference in the amplitude of the tensile wave is about 1 GPa, which is small compared to the maximum amplitude of 10–15 GPa obtained in our simulations (see Fig. 9).

5.4. Substrate

There are two possible thermo-mechanical damage scenarios in a thin film on a substrate. In the first one, the frontal tensile wave is sufficiently strong to cause material rapture, before the superposition with the pressure wave coming from the Ru-Si interface occurs. In the second scenario the frontal tensile wave is too weak to cause damage, but after the superposition with a rear-side wave, the resulting tensile stress can be sufficiently high. In that case damage starts in the region deeper than the middle of the film thickness [26]. Therefore, experimentally determined crater depths, defined by the energy localization, indicate that the first scenario is realized, making the role of a substrate negligible on the timescale before the material rapture occurs.

6. Conclusions

We performed a comparative experimental and theoretical study of ablation in Ru thin films irradiated with single-shot femtosecond laser pulses at various photon energies: 1.5 eV (optical), 92 eV (XUV), 7 and 12 keV (hard X-rays). Optical irradiation was set at normal incidence conditions, while grazing incidence conditions were applied in the XUV and hard X-ray cases. The ablation threshold is found to increase with increasing energy penetration depth. Despite the wide range of experimental irradiation conditions, the ablation craters appear to be very similar with approximately the same depth of 10–20 nm.

Such unexpected similarity in the ablation crater depth and the trend in the ablation threshold are explained with our theoretical analysis using the combination of Monte-Carlo simulations of electron transport and two-temperature hydrodynamics. The non-equilibrium electron cascading processes induced after absorption of XUV and hard X-ray photons play an essential role in spreading the absorbed laser energy in the sample: the higher the photon energy, the deeper the absorbed energy is transported by the cascading electrons. In order to achieve the same absorbed dose in the top part of the sample, where the damage occurs, one needs a higher fluence for higher photon energy.

Although, after the cascading is finished, the deep parts of absorbed energy distribution are different and strongly depend on the photon energy, the energy distributions in the top 10–20 nm are similar for all considered photon energies. We found that the same process determines the near-surface absorbed energy profile for the XUV and hard X-rays cases, namely the many-step decay of the core–shell hole with a release of numerous low-energy Auger electrons. Such Auger electrons can only travel a short distance of less than 10 nm, confining the energy in the vicinity of the surface. One should note that such a mechanism is dominant only for grazing incidence conditions, when the photon absorption depth is smaller than the photoelectron range.

A similar distribution of the absorbed energy in the top 10–20 nm of Ru induces a similar hydrodynamical evolution. With our 2T-HD simulations we show that the thermo-induced pressure waves are generated in the surface region and propagate into the depth of the material. The tensile part of the pressure wave is responsible for the material rapture. The maximum amplitude of the tensile wave reached at the depth of 10–20 nm (where ablation occurs according to the experiment) is similar for all photon energies and equals to 10–15 GPa. That gives us an estimation of the spall strength of Ru at ultra-high strain rates of $10^{10}\ \mathrm{s}^{-1}$.

Acknowledgements

The authors thank Ryszard Sobierajski, Jaromir Chalupsky and Andrew Aquila for the useful discussions and for providing additional information regarding the experiments at SACLA. The authors thank Ludger Inhester for the help with the XATOM simulations. IMi, IMa, EL and FB acknowledge support from the Industrial Focus Group XUV Optics of the MESA + Institute for Nanotechnology of the University of Twente; the industrial partners ASML, Carl Zeiss SMT GmbH, and Malvern Panalytical, the Province of Overijssel, and the Netherlands Organisation for Scientific Research (NWO).

The work of IMi, IMa, EL and FB was supported by the Dutch Topconsortia Kennis en Innovatie (TKI) Program on High-Tech Systems and Materials [14 HTSM 05]; The work of NM was supported by the Czech Ministry of Education, Youth and Sports, Czech Republic [grants numbers LTT17015, LM2015083]. The work of VKh and YuP was supported by the State assignment No. 0033-2019-0007. The work of VZ and NI was supported by the Russian Science Foundation [Grant No. 19-19-00697].

References

[1] R. Ernstorfer, M. Harb, C.T. Hebeisen, G. Sciaini, T. Dartigalongue, R.D. Miller, The formation of warm dense matter: experimental evidence for electronic bond hardening in gold, Science 323 (5917) (2009) 1033–1037, https://doi.org/10.1126/science.1162697.

[2] E. García Saiz, G. Gregori, D.O. Gericke, J. Vorberger, B. Barbrel, R.J. Clarke, R.R. Freeman, S.H. Glenzer, F.Y. Khattak, M. Koenig, O.L. Landen, D. Neely, P. Neumayer, M.M. Notley, A. Pelka, D. Price, M. Roth, M. Schollmeier, C. Spindloe, R.L. Weber, L. van Woerkom, K. Wünsch, D. Riley, Probing warm dense lithium by inelastic X-ray scattering, Nat. Phys. 4 (12) (2008) 940, https://doi.org/10.1038/nphys1103.

[3] N. Medvedev, B. Ziaja, Multistep transition of diamond to warm dense matter state revealed by femtosecond X-ray diffraction, Scient. Rep. 8 (1) (2018) 5284, https://doi.org/10.1038/s41598-018-23632-8.

[4] F. Graziani, M.P. Desjarlais, R. Redmer, S.B. Trickey, Frontiers and Challenges in Warm Dense Matter Vol. 96 Springer Science & Business, 2014.

[5] B.N. Chichkov, C. Momma, S. Nolte, F. Von Alvensleben, A. Tünnermann, Femtosecond, picosecond and nanosecond laser ablation of solids, Appl. Phys. A 63 (2) (1996) 109–115, https://doi.org/10.1007/BF01567637.

[6] X. Liu, D. Du, G. Mourou, Laser ablation and micromachining with ultrashort laser pulses, IEEE J. Quant. Electron. 33 (10) (1997) 1706–1716, https://doi.org/10.1109/3.631270.

[7] J. Hermann, M. Benfarah, G. Coustillier, S. Bruneau, E. Axente, J.-F. Guillemoles, M. Sentis, P. Alloncle, T. Itina, Selective ablation of thin films with short and ultrashort laser pulses, Appl. Surf. Sci. 252 (13) (2006) 4814–4818, https://doi.org/10.1016/j.apsusc.2005.06.057.

[8] S.I. Ashitkov, N. Inogamov, V.V. Zhakhovskii, Y.N. Emirov, M.B. Agranat, I. Oleinik, S.I. Anisimov, V.E. Fortov, Formation of nanocavities in the surface layer of an aluminum target irradiated by a femtosecond laser pulse, JETP Lett. 95 (4) (2012) 176–181, https://doi.org/10.1134/S0021364012040042.

[9] M.V. Shugaev, C. Wu, O. Armbruster, A. Naghilou, N. Brouwer, D.S. Ivanov, T.J.-Y. Derrien, N.M. Bulgakova, W. Kautek, B. Rethfeld, L.V. Zhigilei, Fundamentals of ultrafast laser-material interaction, MRS Bull. 41 (12) (2016) 960–968, https://doi.org/10.1557/mrs.2016.274.

[10] M.V. Shugaev, I. Gnilitskyi, N.M. Bulgakova, L.V. Zhigilei, Mechanism of single-pulse ablative generation of laser-induced periodic surface structures, Phys. Rev. B 96 (20) (2017) 205429, https://doi.org/10.1103/PhysRevB.96.205429.

[11] A.R. Khorsand, R. Sobierajski, E. Louis, S. Bruijn, E.D. van Hattum, R.W.E. van de Kruijs, M. Jurek, D. Klinger, J.B. Pelka, L. Juha, T. Burian, J. Chalupsky, J. Cihelka, V. Hajkova, L. Vysin, U. Jastrow, N. Stojanovic, S. Toleikis, H. Wabnitz, K. Tiedtke, K. Sokolowski-Tinten, U. Shymanovich, J. Krzywinski, S. Hau-Riege, R. London, A. Gleeson, E.M. Gullikson, F. Bijkerk, Single shot damage mechanism of mo/si multilayer optics under intense pulsed xuv-exposure, Opt. Exp. 18 (2) (2010) 700–712, https://doi.org/10.1364/OE.18.000700.

[12] I.A. Makhotkin, R. Sobierajski, J. Chalupský, K. Tiedtke, G. de Vries, M. Störmer, F. Scholze, F. Siewert, R.W.E. van de Kruijs, I. Milov, E. Louis, I. Jacyna, M. Jurek, D. Klinger, L. Nittler, Y. Syryanyy, L. Juha, V. Hájková, V. Vozda, T. Burian, K. Saksl, B. Faatz, B. Keitel, E. Plönjes, S. Schreiber, S. Toleikis, R. Loch, M. Hermann, S. Strobel, H.-K. Nienhuys, G. Gwalt, T. Mey, H. Enkisch, Experimental study of EUV mirror radiation damage resistance under long-term free-electron laser exposures below the single-shot damage threshold, J. Synchrotr. Radiat. 25 (1) (2018) 77–84, https://doi.org/10.1107/S1600577517017362.

[13] R. Follath, T. Koyama, V. Lipp, N. Medvedev, K. Tono, H. Ohashi, L. Patthey, M. Yabashi, B. Ziaja, X-ray induced damage of b 4 c-coated bilayer materials under various irradiation conditions, Scient. Rep. 9 (1) (2019) 2029, https://doi.org/10.1038/s41598-019-38556-0.

[14] J. Pelka, R. Sobierajski, D. Klinger, W. Paszkowicz, J. Krzywinski, M. Jurek, D. Zymierska, A. Wawro, A. Petroutchik, L. Juha, V. Hajkova, J. Cihelka, J. Chalupsky, T. Burian, L. Vysin, S. Toleikis, K. Sokolowski-Tinten, N. Stojanovic, U. Zastrau, R. London, S. Hau-Riege, C. Riekel, R. Davies, M. Burghammer, E. Dynowska, W. Szuszkiewicz, W. Caliebe, R. Nietubyc, Damage in solids irradiated by a single shot of xuv free-electron laser: irreversible changes investigated using X-ray microdiffraction, atomic force microscopy and nomarski optical microscopy, Radiat. Phys. Chem. 78 (10) (2009) S46–S52, https://doi.org/10.1016/j.radphyschem.2009.06.006.

[15] T. Koyama, H. Yumoto, T. Miura, K. Tono, T. Togashi, Y. Inubushi, T. Katayama, J. Kim, S. Matsuyama, M. Yabashi, K. Yamauchi, H. Ohashi, Damage threshold of coating materials on X-ray mirror for X-ray free electron laser, Rev. Scient. Instrum. 87 (5) (2016) 051801, https://doi.org/10.1063/1.4950723.

[16] T. Koyama, H. Yumoto, Y. Senba, K. Tono, T. Sato, T. Togashi, Y. Inubushi,

T. Katayama, J. Kim, S. Matsuyama, H. Mimura, M. Yabashi, K. Yamauchi, H. Ohashi, T. Ishikawa, Investigation of ablation thresholds of optical materials using 1-µm-focusing beam at hard X-ray free electron laser, Opt. Exp. 21 (13) (2013) 15382–15388, https://doi.org/10.1364/OE.21.015382.

[17] S. Dastjani Farahani, J. Chalupsky, T. Burian, H. Chapman, A. Gleeson, V. Hajkoya, L. Juha, M. Jurek, D. Klinger, H. Sinn, R. Sobierajski, M. Störmer, K. Tiedtke, S. Toleikis, T. Tschentscher, H. Wabnitz, J. Gaudin, Damage threshold of amorphous carbon mirror for 177 ev fel radiation, Nucl. Instrum. Methods Phys. Res. Sect. A: Acceler., Spectrom., Detect. Assoc. Equip. 635 (1) (2011) S39–S42, https://doi.org/10.1016/j.nima.2010.10.133.

[18] J. Krzywinski, D. Cocco, S. Moeller, D. Ratner, Damage threshold of platinum coating used for optics for self-seeding of soft X-ray free electron laser, Opt. Exp. 23 (5) (2015) 5397–5405, https://doi.org/10.1364/OE.23.005397.

[19] I.A. Makhotkin, I. Milov, J. Chalupský, K. Tiedtke, H. Enkisch, G. de Vries, F. Scholze, F. Siewert, J.M. Sturm, K.V. Nikolaev, R.W.E. van de Kruijs, M.A. Smithers, H.A.G.M. van Wolferen, E.G. Keim, E. Louis, I. Jacyna, M. Jurek, D. Klinger, J.B. Pelka, L. Juha, V. Hájková, V. Vozda, T. Burian, K. Saksl, B. Faatz, B. Keitel, E. Plönjes, S. Schreiber, S. Toleikis, R. Loch, M. Hermann, S. Strobel, R. Donker, T. Mey, R. Sobierajski, Damage accumulation in thin ruthenium films induced by repetitive exposure to femtosecond xuv pulses below the single-shot ablation threshold, JOSA B 35 (11) (2018) 2799–2805, https://doi.org/10.1364/JOSAB.35.002799.

[20] U. Zastrau, T. Burian, J. Chalupsky, T. Döppner, T. Dzelzainis, R. Fäustlin, C. Fortmann, E. Galtier, S. Glenzer, G. Gregori, L. Juha, H. Lee, R. Lee, C. Lewis, N. Medvedev, B. Nagler, A. Nelson, D. Riley, F. Rosmej, S. Toleikis, T. Tschentscher, I. Uschmann, S. Vinko, J. Wark, T. Whitcher, E. Förster, Xuv spectroscopic characterization of warm dense aluminum plasmas generated by the free-electron-laser flash, Laser Part. Beams 30 (1) (2012) 45–56, https://doi.org/10.1017/S026303461100067X.

[21] A. Aquila, R. Sobierajski, C. Ozkan, V. Hájková, T. Burian, J. Chalupský, L. Juha, M. Störmer, S. Bajt, M.T. Klepka, P. Dłużewski, K. Morawiec, H. Ohashi, T. Koyama, K. Tono, Y. Inubushi, M. Yabashi, H. Sinn, T. Tschentscher, A.P. Mancuso, J. Gaudin, Fluence thresholds for grazing incidence hard x-ray mirrors, Appl. Phys. Lett. 106 (24) (2015) 241905, https://doi.org/10.1063/1.4922380.

[22] O. Peyrusse, J.-M. André, P. Jonnard, J. Gaudin, Modeling of the interaction of an X-ray free-electron laser with large finite samples, Phys. Rev. E 96 (4) (2017) 043205, https://doi.org/10.1103/PhysRevE.96.043205.

[23] I. Milov, I.A. Makhotkin, R. Sobierajski, N. Medvedev, V. Lipp, J. Chalupský, J.M. Sturm, K. Tiedtke, G. de Vries, M. Störmer, F. Siewert, R. van de Kruijs, E. Louis, I. Jacyna, M. Jurek, L. Juha, V. Hájková, V. Vozda, T. Burian, K. Saksl, B. Faatz, B. Keitel, E. Plönjes, S. Schreiber, S. Toleikis, R. Loch, M. Hermann, S. Strobel, H.-K. Nienhuys, G. Gwalt, T. Mey, H. Enkisch, F. Bijkerk, Mechanism of single-shot damage of Ru thin films irradiated by femtosecond extreme UV free-electron laser, Opt. Exp. 26 (15) (2018) 19665, https://doi.org/10.1364/OE.26.019665.

[24] A. Aquila, R. Sobierajski, C. Ozkan, V. Hájková, T. Burian, J. Chalupský, L. Juha, M. Störmer, S. Bajt, M.T. Klepka, P. Dluzewski, K. Morawiec, H. Ohashi, T. Koyama, K. Tono, Y. Inubushi, M. Yabashi, H. Sinn, T. Tschentscher, A.P. Mancuso, J. Gaudin, Erratum: "Fluence thresholds for grazing incidence hard X-ray mirrors" [Appl. Phys. Lett. 106, 241905 (2015)], Appl. Phys. Lett. 115 (5) (2019) 59901, https://doi.org/10.1063/1.5114937.

[25] D.S. Ivanov, L.V. Zhigilei, Combined atomistic-continuum modeling of short-pulse laser melting and disintegration of metal films, Phys. Rev. B 68 (6) (2003) 064114, https://doi.org/10.1103/PhysRevB.68.064114.

[26] B.J. Demaske, V.V. Zhakhovsky, N.A. Inogamov, I.I. Oleynik, Ablation and spallation of gold films irradiated by ultrashort laser pulses, Phys. Rev. B 82 (6) (2010) 064113, https://doi.org/10.1103/PhysRevB.82.064113.

[27] S. Anisimov, N. Inogamov, Y.V. Petrov, V. Khokhlov, V. Zhakhovskii, K. Nishihara, M. Agranat, S. Ashitkov, P. Komarov, Interaction of short laser pulses with metals at moderate intensities, Appl. Phys. A 92 (4) (2008) 939–943, https://doi.org/10.1007/s00339-008-4607-y.

[28] V. Lipp, N. Medvedev, B. Ziaja, Classical Monte-Carlo simulations of x-ray induced electron cascades in various materials, no. May 2017, 2017, p. 102360H. https://doi.org/10.1117/12.2267939.

[29] Y. Petrov, K. Migdal, N. Inogamov, V. Khokhlov, D. Ilnitsky, I. Milov, N. Medvedev, V. Lipp, V. Zhakhovsky, Ruthenium under ultrafast laser excitation: model and dataset for equation of state, conductivity, and electron-ion coupling, Data in Brief.

[30] S. Nolte, C. Momma, H. Jacobs, A. Tünnermann, B.N. Chichkov, B. Wellegehausen, H. Welling, Ablation of metals by ultrashort laser pulses, JOSA B 14 (10) (1997) 2716–2722, https://doi.org/10.1364/JOSAB.14.002716.

[31] K. Sokolowski-Tinten, J. Bialkowski, A. Cavalleri, D. von der Linde, A. Oparin, J. Meyer-ter Vehn, S.I. Anisimov, Transient states of matter during short pulse laser ablation, Phys. Rev. Lett. 81 (1) (1998) 224–227, https://doi.org/10.1103/PhysRevLett. 81.224.

[32] V. Zhakhovskii, N. Inogamov, Y. Petrov, S. Ashitkov, K. Nishihara, Molecular dynamics simulation of femtosecond ablation and spallation with different interatomic potentials, Appl. Surf. Sci. 255 (24) (2009) 9592–9596, https://doi.org/10.1016/j.apsusc.2009.04.082.

[33] L.V. Zhigilei, Z. Lin, D.S. Ivanov, Atomistic modeling of short pulse laser ablation of metals: connections between melting, spallation, and phase explosion, J. Phys. Chem. C 113 (27) (2009) 11892–11906, https://doi.org/10.1021/jp902294m.

[34] M.V. Shugaev, C. Wu, O. Armbruster, A. Naghilou, N. Brouwer, D.S. Ivanov, T.J. Derrien, N.M. Bulgakova, W. Kautek, B. Rethfeld, L.V. Zhigilei, Fundamentals of ultrafast laser-material interaction, MRS Bull. 41 (12) (2016) 960–968, https://doi.org/10.1557/mrs.2016.274.

[35] W. Ackermann, G. Asova, V. Ayvazyan, A. Azima, N. Baboi, J. Bähr, V. Balandin, B. Beutner, A. Brandt, A. Bolzmann, R. Brinkmann, O.I. Brovko, M. Castellano, P. Castro, L. Catani, E. Chiadroni, S. Choroba, A. Cianchi, J.T. Costello, D. Cubaynes, J. Dardis, W. Decking, H. Delsim-Hashemi, A. Delserieys, G. Di Pirro, M. Dohlus, S. Düsterer, A. Eckhardt, H.T. Edwards, B. Faatz, J. Feldhaus, K. Flöttmann, J. Frisch, L. Fröhlich, T. Garvey, U. Gensch, C. Gerth, M. Görler, N. Golubeva, H.-J. Grabosch, M. Grecki, O. Grimm, K. Hacker, U. Hahn, J.H. Han, K. Honkavaara, T. Hott, M. Hüning, Y. Ivanisenko, E. Jaeschke, W. Jalmuzna, T. Jezynski, R. Kammering, V. Katalev, K. Kavanagh, E.T. Kennedy, S. Khodyachykh, K. Klose, V. Kocharyan, M. Körfer, M. Kollewe, W. Koprek, S. Korepanov, D. Kostin, M. Krassilnikov, G. Kube, M. Kuhlmann, C.L.S. Lewis, L. Lilje, T. Limberg, D. Lipka, F. Löhl, H. Luna, M. Luong, M. Martins, M. Meyer, P. Michelato, V. Miltchev, W.D. Möller, L. Monaco, W.F.O. Müller, O. Napieralski, O. Napoly, P. Nicolosi, D. Nölle, T. Nuñez, A. Oppelt, C. Pagani, R. Paparella, N. Pchalek, J. Pedregosa-Gutierrez, B. Petersen, B. Petrosyan, G. Petrosyan, L. Petrosyan, J. Pflüger, E. Plönjes, L. Poletto, K. Pozniak, E. Prat, D. Proch, P. Pucyk, P. Radcliffe, H. Redlin, K. Rehlich, M. Richter, M. Roehrs, J. Roensch, R. Romaniuk, M. Ross, J. Rossbach, V. Rybnikov, M. Sachwitz, E.L. Saldin, W. Sandner, H. Schlarb, B. Schmidt, M. Schmitz, P. Schmüser, J.R. Schneider, E.A. Schneidmiller, S. Schnepp, S. Schreiber, M. Seidel, D. Sertore, A.V. Shabunov, C. Simon, S. Simrock, E. Sombrowski, A.A. Sorokin, P. Spanknebel, R. Spesyvtsev, L. Staykov, B. Steffen, F. Stephan, F. Stulle, H. Thom, K. Tiedtke, M. Tischer, S. Toleikis, R. Treusch, D. Trines, I. Tsakov, E. Vogel, T. Weiland, H. Weise, M. Wellhöfer, M. Wendt, I. Will, A. Winter, K. Wittenburg, W. Wurth, P. Yeates, M. V. Yurkov, I. Zagorodnov, K. Zapfe, Operation of a free-electron laser from the extreme ultraviolet to the water window, Nat. Photon. 1 (6) (2007) 336–342. https://doi.org/10.1038/nphoton.2007.76.

[36] D. Pile, X-rays: first light from sacla, Nat. Photon. 5 (8) (2011) 456, https://doi.org/10.1038/nphoton.2011.178.

[37] J.M. Liu, Simple technique for measurements of pulsed Gaussian-beam spot sizes, Opt. Lett. 7 (5) (1982) 196, https://doi.org/10.1364/OL.7.000196.

[38] J. Chalupský, J. Krzywinski, L. Juha, V. Hájková, J. Cihelka, T. Burian, L. Vyšín, J. Gaudin, A. Gleeson, M. Jurek, A.R. Khorsand, D. Klinger, H. Wabnitz, R. Sobierajski, M. Störmer, K. Tiedtke, S. Toleikis, Spot size characterization of focused non-Gaussian X-ray laser beams, Opt. Exp. 18 (26) (2010) 27836, https://doi.org/10.1364/OE.18.027836.

[39] J. Chalupský, T. Burian, V. Hájková, L. Juha, T. Polcar, J. Gaudin, M. Nagasono, R. Sobierajski, M. Yabashi, J. Krzywinski, Fluence scan: an unexplored property of a laser beam, Opt. Exp. 21 (22) (2013) 26363, https://doi.org/10.1364/OE.21.026363.

[40] M. Wen, I.V. Kozhevnikov, F. Siewert, A.V. Buzmakov, C. Xie, Q. Huang, Z. Wang, L. Samoylova, H. Sinn, Effect of the surface roughness on X-ray absorption by mirrors operating at extremely small grazing angles, Opt. Exp. 26 (16) (2018) 21003–21018, https://doi.org/10.1364/OE.26.021003.

[41] B. Ziaja, R.A. London, J. Hajdu, Unified model of secondary electron cascades in diamond, J. Appl. Phys. 97 (6) (2005) 064905, https://doi.org/10.1063/1.1853494.

[42] K. Mecseki, H. Höppner, M. Büscher, V. Tkachenko, N. Medvedev, J.J. Bekx, V. Lipp, P. Piekarz, M. Windeler, J.W.G. Tisch, D.J. Walke, M. Nakatsutsumi, M.J. Prandolini, J.M. Glownia, T. Sato, M. Sikorski, M. Chollet, U. Teubner, J. Robinson, S. Toleikis, B. Ziaja, F. Tavella, Hard x-ray induced fast secondary electron cascading processes in solids, Appl. Phys. Lett. 113 (11) (2018) 114102, https://doi.org/10.1063/1.5046070.

[43] D. Cullen, A survey of atomic binding energies for use in epics2017, Tech. rep., Vienna, 2018.

[44] Y.-K. Kim, M.E. Rudd, Binary-encounter-dipole model for electron-impact ionization, Phys. Rev. A 50 (5) (1994) 3954, https://doi.org/10.1103/PhysRevA.50.3954.

[45] T.M. Jenkins, W.R. Nelson, A. Rindi, Monte Carlo Transport of Electrons and Photons Vol. 38 Springer Science & Business Media, 2012.

[46] I. Milov, V. Lipp, N. Medvedev, I.A. Makhotkin, E. Louis, F. Bijkerk, Modeling of XUV-induced damage in Ru films: the role of model parameters, Josa B 35 (10) (2018) B43–B53, https://doi.org/10.1364/JOSAB.35.000B43.

[47] S.I. Anisimov, B.L. Kapeliovich, T.L. Perel'man, Electron emission from metal surfaces exposed to ultrashort laser pulses, Sov. Phys. JETP 39 (1974) 375–377.

[48] Y.V. Petrov, N.A. Inogamov, K.P. Migdal, Thermal conductivity and the electron-ion heat transfer coefficient in condensed media with a strongly excited electron subsystem, JETP Lett. 97 (1) (2013) 20–27, https://doi.org/10.1134/S0021364013010098.

[49] N.A. Inogamov, Y.V. Petrov, V.V. Zhakhovsky, V.A. Khokhlov, B.J. Demaske, S.I. Ashitkov, K.V. Khishchenko, K.P. Migdal, M.B. Agranat, S.I. Anisimov, V.E. Fortov, Two-temperature thermodynamic and kinetic properties of transition metals irradiated by femtosecond lasers, AIP Conf. Proc. 1464 (2012) 593–608, https://doi.org/10.1063/1.4739912.

[50] B. Rethfeld, D.S. Ivanov, M.E. Garcia, S.I. Anisimov, Modelling ultrafast laser ablation, J. Phys. D 50 (19) (2017) 193001, https://doi.org/10.1088/1361-6463/50/19/193001.

[51] Y.B. Zel'dovich, Y.P. Raizer, Physics of Shock Waves and High-temperature Hydrodynamic Phenomena, Academic Press, NY, 1967, https://doi.org/10.1016/B978-0-12-395672-9.X5001-2.

[52] M.L. Wilkins, Computer Simulation of Dynamic Phenomena, Springer Science & Business Media, 2013.

[53] H.B. Michaelson, The work function of the elements and its periodicity, J. Appl. Phys. 48 (11) (1977) 4729–4733, https://doi.org/10.1063/1.323539.

[54] N. Medvedev, Femtosecond X-ray induced electron kinetics in dielectrics: application for FEL-pulse-duration monitor, Appl. Phys. B 118 (3) (2015) 417–429, https://doi.org/10.1007/s00340-015-6005-4.

[55] L.V. Zhigilei, Z. Lin, D.S. Ivanov, Atomistic modeling of short pulse laser ablation of metals: connections between melting, spallation, and phase explosion, J. Phys.

Chem. C 113 (27) (2009) 11892–11906.

[56] S. Ashitkov, V. Zhakhovsky, N. Inogamov, P. Komarov, M. Agranat, G. Kanel, The behavior of iron under ultrafast shock loading driven by a femtosecond laser, AIP Conference Proceedings, vol. 1793, AIP Publishing, 2017, p. 100035, , https://doi.org/10.1063/1.4971660.

[57] J.H. Rose, J.R. Smith, F. Guinea, J. Ferrante, Universal features of the equation of state of metals, Phys. Rev. B 29 (6) (1984) 2963, https://doi.org/10.1103/PhysRevB.29.2963.

[58] E. Cordfunke, R. Konings, The high temperature thermophysical properties of ruthenium and palladium, Thermochim. acta 139 (1989) 99–106, https://doi.org/10.1016/0040-6031(89)87013-3.

[59] N. Medvedev, Z. Li, B. Ziaja, Thermal and nonthermal melting of silicon under femtosecond X-ray irradiation, Phys. Rev. B 91 (5) (2015) 054113, https://doi.org/10.1103/PhysRevB.91.054113.

[60] N. Medvedev, V. Tkachenko, V. Lipp, Z. Li, B. Ziaja, Various damage mechanisms in carbon and silicon materials under femtosecond X-ray irradiation, https://doi.org/10.1051/fopen/2018003.

[61] A.E. Morris, H.A. Fine, G. Geiger, Handbook on Material and Energy Balance Calculations in Material Processing, Includes CD-ROM, John Wiley Sons, 2011.

[62] G. Kanel, S. Razorenov, A. Bogatch, A. Utkin, V. Fortov, D. Grady, Spall fracture properties of aluminum and magnesium at high temperatures, J. Appl. Phys. 79 (11) (1996) 8310–8317, https://doi.org/10.1063/1.362542.

[63] T. De Rességuier, L. Signor, A. Dragon, P. Severin, M. Boustie, Spallation in laser shock-loaded tin below and just above melting on release, J. Appl. Phys. 102 (7) (2007) 073535, https://doi.org/10.1063/1.2795436.

[64] M.B. Agranat, S.I. Anisimov, S.I. Ashitkov, V.V. Zhakhovskii, N. Inogamov, P.S. Komarov, A.V. Ovchinnikov, V.E. Fortov, V.A. Khokhlov, V.V. Shepelev, Strength properties of an aluminum melt at extremely high tension rates under the action of femtosecond laser pulses, JETP Lett. 91 (9) (2010) 471–477, https://doi.org/10.1134/S0021364010090080.

[65] Y. Cai, H. Wu, S. Luo, Spall strength of liquid copper and accuracy of the acoustic method, J. Appl. Phys. 121 (10) (2017) 105901, https://doi.org/10.1063/1.4978251.

[66] S.-K. Son, L. Young, R. Santra, et al., Impact of hollow-atom formation on coherent x-ray scattering at high intensity, Phys. Rev. A 83 (3) (2011) 033402, https://doi.org/10.1103/PhysRevA.83.033402.

[67] S.-K. Son, R. Santra, Monte carlo calculation of ion, electron, and photon spectra of xenon atoms in X-ray free-electron laser pulses, Phys. Rev. A 85 (6) (2012) 063415, https://doi.org/10.1103/PhysRevA.85.063415.

[68] K. Toyota, S.-K. Son, R. Santra, Interplay between relativistic energy corrections and resonant excitations in X-ray multiphoton ionization dynamics of xe atoms, Phys. Rev. A 95 (4) (2017) 043412, https://doi.org/10.1103/PhysRevA.95.043412.

[69] B. Ziaja, D. van der Spoel, A. Szöke, J. Hajdu, Auger-electron cascades in diamond and amorphous carbon, Phys. Rev. B 64 (21) (2001) 214104, https://doi.org/10.1103/PhysRevB.64.214104.

[70] T. Tachibana, Z. Jurek, H. Fukuzawa, K. Motomura, K. Nagaya, S. Wada, P. Johnsson, M. Siano, S. Mondal, Y. Ito, M. Kimura, T. Sakai, K. Matsunami, H. Hayashita, J. Kajikawa, X.-J. Liu, E. Robert, C. Miron, R. Feifel, J.P. Marangos, K. Tono, Y. Inubushi, M. Yabashi, S.-K. Son, B. Ziaja, M. Yao, R. Santra, K. Ueda, Nanoplasma formation by high intensity hard X-rays, Scient. Rep. 5 (2015) 10977, https://doi.org/10.1038/srep10977.

[71] N.A. Inogamov, V.V. Zhakhovsky, S.I. Ashitkov, V.A. Khokhlov, V.V. Shepelev, P.S. Komarov, A.V. Ovchinnikov, D.S. Sitnikov, Y.V. Petrov, M.B. Agranat, S.I. Anisimov, V.E. Fortov, Laser acoustic probing of two-temperature zone created by femtosecond pulse, Contribut. Plasma Phys. 51 (4) (2011) 367–374, https://doi.org/10.1002/ctpp.201010111.

[72] V. Zhakhovskii, K. Nishihara, Y. Fukuda, S. Shimojo, T. Akiyama, S. Miyanaga, H. Sone, H. Kobayashi, E. Ito, Y. Seo, M. Tamura, Y. Ueshima, A new dynamical domain decomposition method for parallel molecular dynamics simulation, in: IEEE International Symposium on Cluster Computing and the Grid, Vol. 2, 2005, pp. 848–854. https://doi.org/10.1109/CCGRID.2005.1558650.

[73] V. Zhakhovsky, K. Migdal, N. Inogamov, S. Anisimov, Md simulation of steady shock-wave fronts with phase transition in single-crystal iron, AIP Conference Proceedings, Vol. 1793 AIP Publishing, 2017, p. 070003, , https://doi.org/10.1063/1.4971591.

[74] Ruthenium interatomic potential in the framework of embedded atom model is obtained by V. Zhakhovsky using the stress-matching method [30, 69], see also https://www.researchgate.net/project/Development-of-interatomic-EAM-potentials. Submitted to Appl. Surf. Sci. (2019).